Geophysical Journal International

Geophys. J. Int. (2020) **220,** 267–277
Advance Access publication 2019 October 07
GJI Seismology

doi: 10.1093/gji/ggz450

First 2-D intrinsic and scattering attenuation images of Mt Etna volcano and surrounding region from active seismic data

Jesús M. Ibáñez [1,2,3] Ignacio Castro-Melgar [3] Ornella Cocina,[2] Luciano Zuccarello [1,3] Stefano Branca,[2] Edoardo Del Pezzo [1,4] and Janire Prudencio[1,3]

[1] *Andalusian Institute of Geophysics, University of Granada, Profesor Clavera* 12, 18071 *Granada, Spain. E-mail: jibanez@ugr.es*
[2] *Istituto Nazionale di Geofisica e Vulcanologia, Osservatorio Etneo,* 95125 *Catania, Italy*
[3] *Department of Theoretical Physics and Cosmos, Faculty of Science, University of Granada,* 18071 *Granada, Spain*
[4] *Istituto Nazionale di Geofisica e Vulcanologia, Osservatorio Vesuviano,* 80124 *Naples, Italy*

Accepted 2019 October 4. Received 2019 October 2; in original form 2019 June 4

SUMMARY

We present 2-D attenuation images of the Mt Etna volcanic region on the basis of separation of intrinsic and scattering effects. The analysis presented here exploits a large active seismic database that fully covers the area under study. We observe that scattering effects dominate over intrinsic attenuation, suggesting that the region is very heterogeneous. Comparison with analyses conducted at other volcanoes reveals that the Mt Etna region is characterized by high intrinsic attenuation, resulting from the presence of large volcanoclastic deposits at shallow depth. The 2-D distributions of intrinsic and scattering anomalies show the presence of regions characterized by high and low attenuation effects, corresponding to several tectonic and volcanic features. In particular, we identify a high attenuation region in the SW sector of the Mt Etna volcanic complex, which is correlated with high seismicity rates and volcanism. This work supports the hypothesis of a link between the dynamics of the SW flank and the recharge of the volcano in the last decades, occurring under the summit crater and, secondarily, the upper South rift zone.

Key words: Structure of the Earth; Tomography; Seismic attenuation; Volcano seismology.

1 INTRODUCTION

Knowledge of the subsurface structure of volcanoes is crucial to successfully model the dynamics of volcanic unrest, and to inform eruption early-warning. Traditionally, the internal structure of volcanic systems is investigated using seismic imaging methods such as 3-D seismic velocity tomography (e.g. Koulakov *et al.* 2016). Recently, seismic attenuation imaging focused on small-scale highly heterogeneous geological structures (Prudencio *et al.* 2015a, b; De Siena *et al.* 2016, 2017) has been extensively applied to provide information on important physical properties of the subsurface that are not characterized by ordinary seismic velocity tomography. The attenuation of seismic waves is mainly affected by inelastic absorption and scattering effects. Both can be associated with different structural properties, including the number and extent of fractures, the structural complexity or presence of heterogeneities (e.g. small and abrupt density and/or velocity changes that influence scattering phenomena), and rheological properties (e.g. thermal states of rocks and the rate of consolidation, which contribute to inelastic absorption). However, it is important to separate the relative influence of both factors in order to correctly interpret heterogeneities in the medium and identify the physical mechanisms producing seismic attenuation.

At present, the most accurate technique for discerning the contributions of scattering versus intrinsic attenuation is based on the Energy Transport Model (classical Boltzmann Integral Equation), or its two asymptotic approximations: (i) the so called Single Scattering Model (Aki & Chouet 1975), which is suitable for almost uniform media and (ii) the Diffusion Model (Wu 1985), used when heterogeneity is high, as in the case of volcanoes (e.g. Wegler & Lühr 2001; Del Pezzo 2008). Dainty & Toksöz (1981) first formulated a technique to fit the Energy Seismogram envelope to the Diffusion Model. Modifications of this technique by Wegler & Lühr (2001) and Wegler (2003) can be used to retrieve nearly unbiased estimates of both intrinsic and scattering attenuation coefficients from a single path seismogram, and hence can be used for imaging purposes. This technique has been applied in a number of studies (e.g. Prudencio *et al.* 2013a; Del Pezzo *et al.* 2016) to obtain separate 2D attenuation images of volcanoes using data from shallow artificial sources whose coda is confined in the first 2–3 km of the crust. Coupled with the use of 2-D Gaussian Space Sensitivity Kernels, Prudencio *et al.* (2013a) used this approach to generate robust and stable images of both intrinsic and scattering attenuation beneath the island of Tenerife. Prudencio *et al.* (2013b) proposed a direct relationship between strong scattering effects and the presence of a potential partial melting body near the surface at Deception Island (Antarctica),

and simultaneously, low intrinsic attenuation effects associated with the contact of a consolidate crystalline basement with the volcanic structure. At Stromboli volcano (Italy), Prudencio *et al.* (2015c) identified two main high attenuation zones, the first corresponding to the centre of the island, where volcanic activity takes place, and the second associated with an area where the ancient volcanic edifice is located. At Mt Asama volcano, Prudencio *et al.* (2017a) identified a zone where both scattering and intrinsic attenuation are present, corresponding to a strong structural contrast associated with the presence of a shallow magma intrusion. At Usu volcano, Japan, a gradient of scattering attenuation is associated with deepening of the basement, while intrinsic attenuation indicates areas of debris avalanche deposits (Prudencio *et al.* 2017b).This method can aslo be applied using passive data generated in the first few kilometres of the crust as Del Pezzo *et al.* (2016, 2018) or De Siena *et al.* (2017) demonstrated. An example of this shallow seismicity application is the study performed at Long Valley Caldera, USA (Prudencio *et al.* 2018). These authors highlighted the hydrothermal system and recent eruptive areas based on high attenuation (both intrinsic and scattering) values.

In this paper, we provide, for the first time, two separate images of intrinsic and scattering attenuation parameters within the upper 2–3 km of crust in the Mt. Etna volcanic region using the data set produced by the TOMO-ETNA seismic experiment (Coltelli *et al.* 2016; Ibañez *et al.* 2016a; Ibañez *et al.* 2016b); in this experiment, air-gun shots were recorded by a very dense temporary seismic network operating over this volcanic area.

The Mt Etna region is a dynamic environment in which continuous structural changes associated with different volcanic stages are observed (Patanè *et al.* 2006). One of the advantages of the present study is that the seismic data used were recorded over a very short-time period (less than 1 month), providing a snapshot of the volcanic structure in the first 2–3 km below the crust. Our results complement a 3-D seismic tomography study performed by Diaz-Moreno *et al.* (2018) using the same data set. Mt Etna is one of the best studied volcanic regions worldwide. Ibáñez *et al.* 2016a and references therein provided a review of the most recent geophysical studies. Del Pezzo *et al.* 2019 and references therein offered a review of its tectonic and seismic framework. Chiarabba *et al.* (2004), De Gori *et al.* (2005), Martinez-Arevalo *et al.* (2005) and Alparone *et al.* (2012) give descriptions and interpretations of tomography images. However, uncertainties remain regarding the nature of several structures of the volcano at all depths.

2 METHOD: ASSUMING A DIFFUSIVE REGIME

Volcanoes are frequently characterized by very heterogeneous geological structures, which are well represented in seismology by diffusive random media (e.g. Wu 1985; Wegler & Lühr 2001; Del Pezzo 2008).

The diffusion approximation of the solution of the Energy Transport Equation is valid when

$$\lambda < lg \ll la, \tag{1}$$

where lambda is the dominant wavelength, and *la* and *lg* are the intrinsic and scattering mean free paths, respectively. In turn, *la* and *lg* can be written as

$$lg = \frac{v Qs}{2\pi f}; la = \frac{v Qi}{2\pi f}, \tag{2}$$

where f is the dominant frequency, v is the wave velocity and Qi and Qs are the intrinsic and scattering quality factors, respectively. For lambda of ∼0.3 km, corresponding to a dominant frequency of 6 Hz with $v = 2.6$ km s^{-1} (value of the theoretical *S*-waves velocity derived from the results of the tomography of Díaz-Moreno *et al.* 2018 using the same set of data in where *Vp* was of 4.4 km s^{-1} and the derived *Vp*/*Vs* ratio was of 1.7), *lg*, as Del Pezzo (2008) indicates, should be greater than 0.3 and much less than 30 km, or, in the same range of frequency and wave speed, *Qs* should be approximately in the range between 30 and 100.

This condition is fulfilled at Mt Etna (e.g. Del Pezzo *et al.* 2019) and, therefore, the diffusion model is an appropriate approximation for the data used in the present study. We thus applied the transport equation in its asymptotic approximation (diffusion model) to separately estimate scattering and intrinsic attenuation coefficients (Sato *et al.* 2012). We followed the fitting procedure described by Wegler & Lühr (2001).

The seismogram energy envelope is described by the diffusion model ($E[r, t]$) as a function of source–receiver distance, r and lapse time, t, through the equation

$$E\ [r, t] = E_0\ (4\pi \mathrm{d}t)^{-p/2} \exp\left[-\frac{r^2}{4\mathrm{d}t} - bt\right], \tag{3}$$

where E_0 is the energy at the source, d is the diffusivity, b is the intrinsic attenuation coefficient and p is a dimensional factor related to the geometrical spreading term as it is described by Dainty & Toksöz (1981) and used by Wegler & Lühr (2001) or Wegler (2003). Coefficients d and b are directly related to Qi and Qs, respectively, through the equations

$$Q_i = \frac{2\pi f}{b} \tag{4}$$

$$Q_s = \frac{2\pi f p d}{v^2} \tag{5}$$

where f is the central frequency of filtered seismograms and v is the half-space velocity.

From the above definitions of the intrinsic and scattering mean free path,

$$la = \frac{v}{b} \text{ and } lg = \frac{pd}{v}. \tag{6}$$

Finally, the total Q can be defined by

$$Q_t^{-1} = Q_i^{-1} + Q_s^{-1}. \tag{7}$$

3 SEISMIC DATA, DATA ANALYSIS AND DATA MAPPING

3.1 Seismic data

The data analysed in this study is a subset of data from the TOMO-ETNA active seismic experiment, which was performed between June and December 2014 (Ibáñez *et al.* 2016a,b). Here, we preliminary selected 9705 air-gun shots fired by the Spanish oceanographic vessel 'Sarmiento de Gamboa' in the Ionian Sea and recorded by 120 inland seismic stations on and around Mt Etna volcano (Fig. 1).

3.2 Data analysis

For each seismogram, intrinsic and scattering coefficients were estimated following the procedure of Prudencio *et al.* (2013a, b, 2015c)

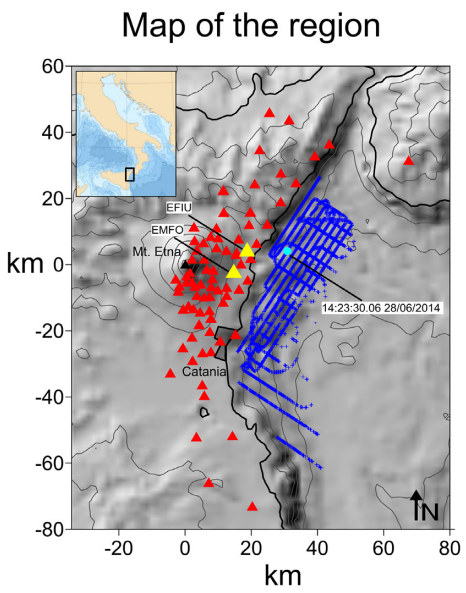

Figure 1. Map of the study region. Red triangles represent the positions of seismic stations used in this study. Blue dots are the locations of the air-gun shots generated during the TOMO-ETNA experiment. The highlighted stations (yellow triangles) and shot (light blue dot) are the stations and shot used as examples in Figs 2 and 3.

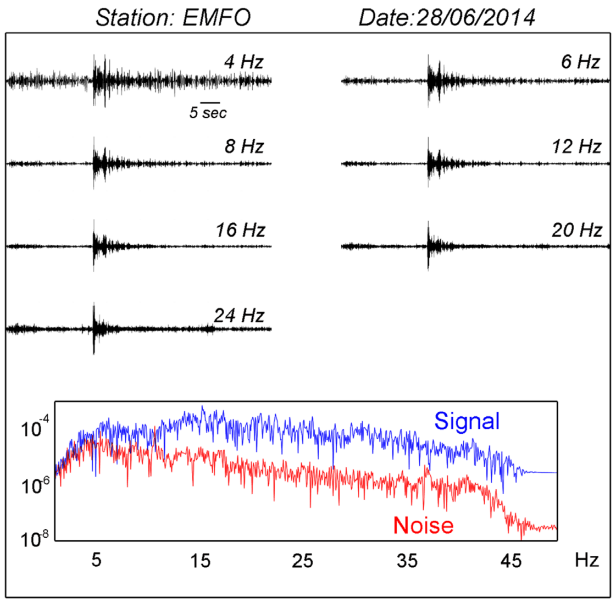

Figure 2. (a) Example seismic records filtered at different frequency bands. (b) Comparison of noise and signal spectra of the same signal; note that the signal-to-noise ratio is high up to 24 Hz. The seismic station and shot are identified in Fig. 1.

in where similar marine data sources were used. The most important steps of the procedure include filtering, signal extraction, water wave extraction, signal envelope and parameter extraction.

3.2.1 *Filtering*

We first analysed the spectra of a selected sample of seismograms to identify the frequency range in which the signal-to-noise ratio is suitable for further analysis. Based on this analysis, seismic signals were filtered at frequency bands centred at 4, 6, 8, 12, 16, 20 and 24 Hz with a bandwidth of $f_c \pm 0.6f_c$, using a Butterworth bandpass filter with eight poles. The signal-to-noise ratio was measured in each seismogram, and all waveforms showing values of less than 2 at the end of the seismogram coda were rejected. The final data set analysed and used to perform our images consisted of 15 961 vertical waveforms for the lowest frequency (4 Hz) and 13 932 vertical waveforms for the highest frequency (24 Hz). The distance range of the selected signals range between 3.8 and 25.9 km. Fig. 2 shows an example filtered seismogram and the corresponding spectrum of the unfiltered signal.

3.2.2 *Signal extraction*

We extracted the portion of the filtered seismograms from the theoretical *S*-wave onset and to a lapse time of 20 s, measured from the origin time. Hence, t_{min} was equal to the theoretically calculated *S*-wave arrival time and t_{max} corresponded to the time interval, which was always 20 s long. Fig. 3 shows the selected signal analysis window. The active seismic source is a pure pressure *P*-wave generated on the surface of the sea, and propagated towards the sea bottom. Therefore it is expected that after to impact the sea bottom only *P* waves should be propagated to the received. However as Yamamoto & Sato (2010) demonstrated, with the exception of a very small portion of the first seismic package, the main part of the seismogram is composed by converted *P* to *S* waves.

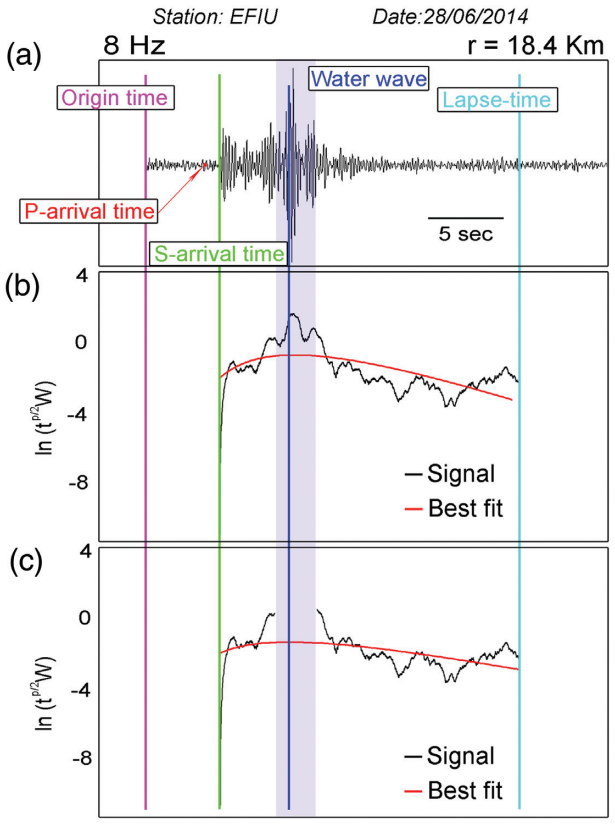

Figure 3. (a) Seismogram of a shot with the water-wave highlighted (dark blue line). The pink line denotes the origin time of the shot; the red arrow indicates the real *P*-wave onset; the green line denotes the theoretically calculated *S*-waves arrival; and the light blue line marks the end of the analysis window. (a) and (b) Comparisons of best fit between the data and model (b) with and (c) without the water-wave energy package.

3.2.3 *Water wave extraction*

The seismic sources were air-gun shots generated on the surface of the sea. This type of signal produces secondary waves that travel directly from the source to the station through the water volume. Previous analysis of similar experiments (Zandomeneghi *et al.* 2009; García-Yeguas *et al.* 2012) has shown that this type of wave has a known propagation velocity and high energy, and is therefore easily identifiable on seismograms. Recently Carmona *et al.* (2015) identified these types of *T* waves in the Mediterranean basin for shallow earthquakes.

The sound speed profile in the Mediterranean area differs from that in open oceans (in the temperate zone), especially for the minimum shape under the thermocline, and the absence of the deep SOFAR channel (Munk *et al.* 1995). As mentioned by Flattè *et al.* (1979) and by Northup & Colborn (1974), the presence of the SOFAR channel, in the ocean environmental, is generally located between 800 and 1200 m. Instead, the location of this propagation channel in the Mediterranean Sea is affected by a surface thermocline and warm deep waters, due to the thermal vertical structure.

The sound speed in the Mediterranean basins is characterized by a seasonal variability with two extremes in February and August (Taburni 2011). During the summer period (August), the water column is characterized by a velocity profile divided into three different layers, from top to bottom: (i) a surface layer with marked decreasing values, heavily influenced by the rapid decrease of temperature; (ii) a minimum velocity value located at the base of the seasonal thermocline and (iii) a slow but steady increase due to the effect of pressure under the thermocline layer (Salon *et al.* 2003). In terms of the propagation of sound waves, this produces a channeled propagation that is constrained below the thermocline. The velocity profile in winter (February) in the northwestern Mediterranean is characterized by a steady increase with depth, due to the homogeneous vertical distribution of water masses, and therefore it is highly influenced by the effect of pressure. Under 600 m, the vertical velocity gradient is almost constant (about 1 m s^{-1} every 60 m of depth, in agreement with the value of 0.0167 s^{-1} calculated by Jensen *et al.* (1994) for an average of Mediterranean profile), due to the main role of the pressure, the temperature and salinity constant values.

We have performed local velocity measurements, related to summer period (the same period in which the TOMO-ETNA experiment was carried out), using the model proposed by Medwin (1975), limited to a 1000 m depth:

$$\begin{aligned} c = {} & 1449.2 + 4.6T - 0.055T^2 + 0.00029T^3 \\ & + (1.34 - 0.01T)(S-35) + 0.016Z \end{aligned} \quad (8)$$

where c is the sound speed (m s^{-1}), T is the temperature (°C), Z is the depth (m) and S is the salinity (p.s.u.). Due to the lack of any CTD casts database from TOMO-ETNA experiment, we have used the temperature, salinity and pressure data provided by NOAA (National Oceanic and Atmospheric Administration) through the World Ocean Database (http://www.nodc.noaa.gov/OC5/SELECT/dbsearch/dbsearch.html). We have selected the parametric profiles measured in the Aeolian archipelago in the months of July and August in order to maintain the same parametric conditions of the TOMO-ETNA experiment time period providing an average sound speed value of 1509 m s^{-1}.

The water waves should be cut off before applying the fitting procedure to retrieve the attenuation parameters. Here, we directly removed them instead of using any kind of filtering since their frequency content was the same as that of the signal under study. We removed the intervals 0.5 s before and 2.5 s after the theoretically estimated first onset of water waves; Fig. 3 illustrates an example of this procedure, which was applied to all seismograms. In Fig. 3(a), a seismogram filtered at 8 Hz clearly shows the water wave (notice its high amplitude with respect to the rest of the seismogram); in Fig. 3(b), we show the bias corresponding to the fit of the observed Energy Envelope to the theoretical Energy Envelope (including the water wave). Finally, Fig. 3(c) shows the fit to the signal modified by removing the water wave interval.

3.2.4 *Parameter estimation*

Seismogram Energy Envelopes were calculated by applying a Hilbert transform to 0.7-s time windows sliding with an overlap of 50 per cent for each frequency band. We fit energy envelopes to eq. (3) by using a least square method to obtain the b and d parameters and, consequently, Qi and Qs. The first term of eq. (3), the trade-off between the b and d parameters were obtained following Mayeda *et al.* (1992) and Akinci *et al.* (1995) using the F distribution at a 70 per cent level of confidence to estimate the uncertainty intervals in parameters. The average measured uncertainty intervals were of 8 and 6 per cent for b and d, respectively. The lack of a severe trade-off between b and d allowed attenuation effects to be estimated independently. We assumed $p = 3$ as the dimension term for body waves (Wegler & Lühr 2001; Wegler 2003) and discarded data with a correlation coefficient between the theoretical model and experimental data of $R < 0.7$. Finally, we used b and d to obtain Qi and Qs using eqs (4) and (5), respectively. Given b and d, the scattering mean free path ($lg = 3d/v$) and the absorption mean free path ($li = v/b$) could also be calculated. The v (S-wave velocity) was set at 2.6 km s^{-1}, as derived from a velocity model calculated for the Etna region by Diaz-Moreno *et al.* (2018), after averaging Vp in the first 3 km and successively dividing for the Vp/Vs ratio, set at 1.7. Fig. 3 shows an example of the data fit.

4 MAPPING PROCEDURE AND RESOLUTION TESTS

4.1 Mapping procedure

The 2-D spatial images were calculated through space-weighting functions describing the spatial sensitivity of observable data to scattering and intrinsic anomalies. A detailed description of the applied methodology is available in Del Pezzo *et al.* (2016); a recent application to Long Valley Caldera can be found in Prudencio *et al.* (2018). Here we give only a brief summary of the procedure.

Functions were estimated using a heuristic approach based on Monte Carlo numerical solutions of the energy transport equation. The weighting functions numerically calculated for each source–receiver couple result were well approximated by

$$\begin{aligned} w\ [x, y, x_r, y_r, x_s, y_s] = {} & \frac{1}{4\pi\delta_x D^2 \delta_y}\ Exp\left[-\frac{\left(x - \frac{x_r + x_s}{2}\right)^2}{2(\delta_x D)^2} \right. \\ & \left. + \frac{\left(y - \frac{y_r + y_s}{2}\right)^2}{0.5(\delta_y D)^2} \right] + \frac{1}{2\pi\delta_x D^2 \delta_y}\ Exp\left[-\frac{(x - x_s)^2}{2(\delta_x D)^2} + \frac{(y - y_s)^2}{2(\delta_y D)^2} \right] \\ & + \frac{1}{2\pi\delta_x D^2 \delta_y}\ Exp\left[-\frac{(x - x_r)^2}{2(\delta_x D)^2} + \frac{(y - y_r)^2}{2(\delta_y D)^2} \right], \end{aligned} \quad (9)$$

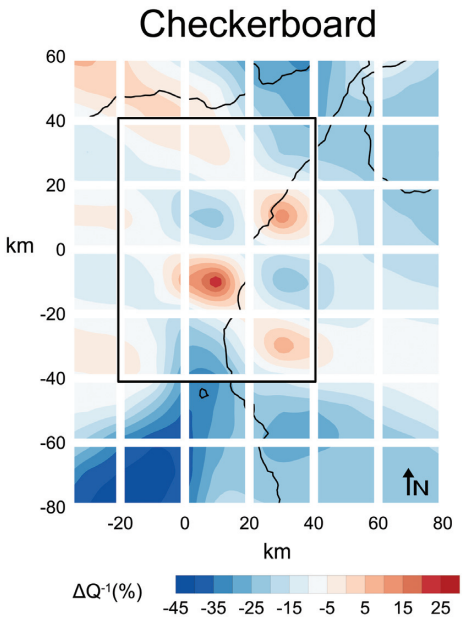

Figure 4. Checkerboard test with 20 × 20 km^2 cell size. We assigned $b = 0.75$ ($Qi = 50$) and $d = 0.21$ ($Qs = 3$) for the high intrinsic and scattering anomalies and $b = 0.4$ ($Qi = 100$) and $d = 23$ ($Qs = 333$) for the low intrinsic and scattering anomalies. The best resolved area is marked by the black contour.

where $w[x, y, x_r, y_r, x_s, y_s]$ fits reasonably well to numerical weighting functions with $\delta_x = \delta_y = 0.2$; δ_x and δ_y represent the spatial aperture of the weighting function in 2-D; and $w[x, y, x0, y0, x_r, y_r]$ is proportional to the probability that, for a source–receiver couple with coordinates at x_s,y_s and x_r,y_r, the estimated parameter couple (Q_i^{-1}, Q_s^{-1}) is effectively the true value at the space point with coordinates x and y. In other words, the value of the attenuation parameter couple Q_i^{-1} and Q_s^{-1} estimated for a single source–receiver is assigned to the whole space volume, weighted by the $w[x,y,x_s,y_s,x_r,y_r]$ associated with the same source–receiver couple. Discretizing the study area or volume in cells, for each cell a number, N, of weighted measures will thus be available, where N is the number of source–receiver couples. However, for many cells, the value of the space weighting functions (SWF) will be extremely small. Finally, the best estimator for the value of $\{Q_i^{-1}, Q_s^{-1}\}$ is calculated under the assumption of Gaussian statistics (the weighted arithmetical average) through the equation

$$Q^{-1}\ [x, y] = \frac{\sum_{k=1}^{N} w\,[x, y, x_{rk}, y_{rk}, x_{sk}, y_{sk}]\, Q_k^{-1}}{\sum_{k=1}^{N} w\,[x, y, x_{rk}, y_{rk}, x_{sk}, y_{sk}]}\ , \qquad (10)$$

where $Q^{-1}[x,y]$ is the estimate in the space point {x,y} (centre cell), k is the source–receiver index spanning from 1 to N, Q_k^{-1} is the kth measurement, and $\{x_{rk}, y_{rk}\}$ and $\{x_{sk}, y_{sk}\}$ are the coordinates of the receiver and source for the kth source–receiver couple, respectively.

4.2 Sensitivity tests

To check resolution and accuracy of the imaging method, sensitivity tests were performed (see Del Pezzo *et al.* 2016 and references therein for details) using the following approach:

(1) An a priory checkerboard-like 2-D structure (otherwise called an input test) was numerically generated and Q^{-1} values were assigned to checkerboard cells such that the contrasts between checkerboard cells were well outside the average per cent uncertainty in the parameter estimation.

(2) For each source–receiver couple of real data, a space weighting-average of the checkerboard structure was calculated, using eq. (8) as the weighting function. It is worth noting that the weighting functions for Qi^{-1} and Qs^{-1} are the same.

(3) The same imaging method used with real data was applied to the above synthetic data set and the results were compared with the input test. Fig. 4 shows an example checkerboard test.

(4) The resolution function (see Appendix A) was calculated. Fig. 5 shows the pattern of the resolution function calculated for the present data set.

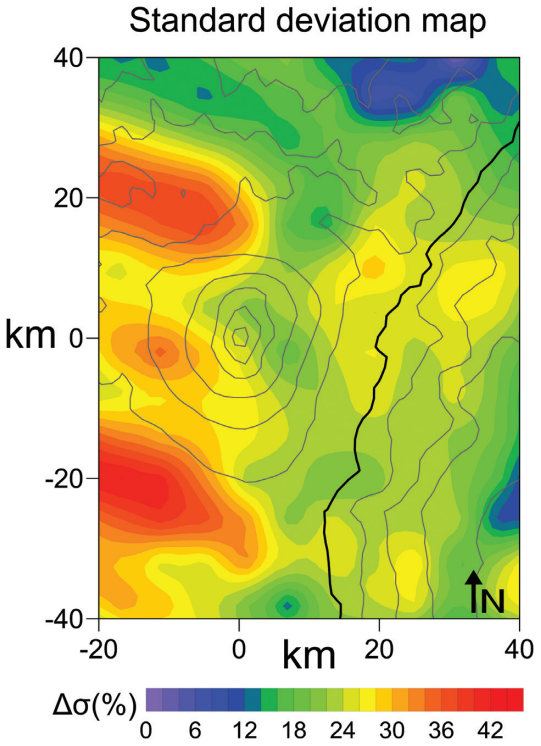

Figure 5. Spatial distribution of calculated standard deviation as a representative quality check of the validity of the obtained images.

5 RESULTS AND DISCUSSION

We interpreted the results by excluding topographic effects, depth dependence and Energy leakage from the upper layers to the deepest structures of the volcano as recently Sanborn & Cormier (2018) confirmed. The reasons for these exclusions are discussed in detail in Prudencio *et al.* (2017a) and Del Pezzo *et al.* (2018). For example, topography is one of the main potential sources of surface wave scattering, being thus potentially a source of bias. As Prudencio *et al.* (2017a) observed, these effects are of a minor order in our approach, and it is even lower when the attenuation is mapped as perturbation. On the other hand, Del Pezzo *et al.* (2018) demonstrated that when shallow active sources are used, 3-D images strongly resemble 2-D images, making this 3-D extension redundant.

5.1 Average intrinsic and scattering attenuation values

Table 1 summarizes average values of Qi, Qs, Qt, lg and li for each central frequency estimated by fitting the diffusion model to the energy envelopes. It is clearly observed that scattering dominates over

Table 1. Average values of b, d, Qi, Qs, Qt, Qi^{-1}, Qs^{-1}, Qt^{-1}, ltr and li for the Mt Etna volcanic region.

	$b \pm$ error	$d \pm$ error	Qi	Qs	Qt	Qi^{-1}	Qs^{-1}	Qt^{-1}	ltr (m)	li (km)
4 Hz	0.719 ± 0.084	1.437 ± 0.085	34	10	7	0.029	0.105	0.134	980	6.1
6 Hz	0.782 ± 0.085	1.383 ± 0.080	48	14	11	0.021	0.073	0.094	943	5.6
8 Hz	0.780 ± 0.084	1.311 ± 0.079	63	19	14	0.016	0.054	0.070	894	5.6
12 Hz	0.775 ± 0.083	1.277 ± 0.079	100	28	22	0.010	0.036	0.046	871	5.7
16 Hz	0.752 ± 0.083	1.238 ± 0.080	143	37	29	0.007	0.027	0.034	844	5.8
20 Hz	0.689 ± 0.079	1.211 ± 0.084	200	50	40	0.005	0.020	0.025	826	6.4
24 Hz	0.637 ± 0.078	1.188 ± 0.089	250	63	50	0.004	0.016	0.020	810	6.9

B: intrinsic attenuation coefficient.
d: diffusivity.
Qi: intrinsic Q value, where Qi^{-1} is the inverse Q value.
Qs: scattering Q value, where Qs^{-1} is the inverse Q value.
Qt: total attenuation Q value, where Qt^{-1} is the inverse Q value.
ltr: transport mean free path measured in metres.
li: absorption length measured in kilometres.

intrinsic attenuation at all frequencies. Seismograms are thus controlled by the presence of geological heterogeneities at the surface. Recently, Del Pezzo *et al.* (2019) analysed regional patterns of intrinsic and scattering attenuation for a region that includes our study area using the Multiple Lapse Time Window Analysis (MLTWA) method (Hoshiba 1991; Akinci *et al.* 1995) with local and regional earthquakes and a source–receiver distance range of between 5 and 70 km. As in the present work, they observed that scattering effects dominate over intrinsic absorption in the Etna region, while their absolute Q-values (see table 1 of their paper) were much larger than those presented here. These differences are explained by the greater depth of the seismic sources analysed. In the present study, seismograms were generated at the surface (air-gun shots) and recorded at epicentral distances between 3 and 25 km; the data provide information on the uppermost part of the crust (i.e. the first few kilometres). In the work of Del Pezzo *et al.* (2019), earthquakes had crustal depths (∼10 km) and were recorded at distances of up to 100 km, providing information on deeper structures. This result implicitly confirms that the Q factor increases with depth in the crust (Ibáñez *et al.* 1991).

The attenuation parameters estimated for the Mt Etna volcanic region are in agreement with values obtained for other volcanic areas where scattering phenomena dominate over intrinsic dissipation (Zieger *et al.* 2016; Prudencio *et al.* 2018, and references therein). Scattering Q values obtained for Mt Etna are almost the same as those obtained for Deception Island (Prudencio *et al.* 2013b) and Mt Asama volcano (Prudencio *et al.* 2017a), but higher than those measured at Stromboli (Prudencio *et al.* 2015c) and Mt Usu (Prudencio *et al.* 2017b). The fact that scattering effects nearly always dominate over intrinsic attenuation provides additional confirmation that volcanoes are heterogeneous geological objects with multiple fracture systems (e.g. Martínez-Arévalo *et al.* 2003) the co-occurrence of molten and rigid structures (e.g. Prudencio *et al.* 2013b; De Siena *et al.* 2014), feeding systems such as dikes and sills (e.g. De Siena *et al.* 2017) and embedded layers of ash and lava flows (e.g. De Siena *et al.* 2016), all alter the geometry of wave fronts producing secondary waves with high intensity. We observe the similar patterns at the Mt Etna, Deception Island, and Mt Asama volcanoes, where evidence for shallow molten material combined with hydrothermal interaction can explain the scattering Q values observed. Nevertheless, Mt Etna shows intrinsic Q values that are smaller than those at other volcanoes analysed using the present technique. This can be explained by the large size of shallow volcanoclastic deposits as De Siena *et al.* (2016) or Wegler (2003) observed in other volcanoes. Mt Etna volcano covers a region of approximately 1200 km^2 and has a total volume of approximately 530 km^3 (Branca & Ferrara 2013; Barreca *et al.* 2018); the edifice consists of a complex volcanic succession made up of massive and scoriaceous lava flows overlying interbedded unwelded and lithified volcanoclastic deposits that rest on the sedimentary and metamorphic rocks that control the rigidity of the shallow regional structure.

5.2 Attenuation image anomalies

The spatial distribution of intrinsic and scattering attenuation estimated with respect to the average values reported in Table 1 are presented in Fig. 5. Intrinsic attenuation is at least 1 order of magnitude lower than scattering attenuation; therefore, total attenuation images are very similar to scattering attenuation images and are not shown. To interpret the images from a geo-volcanological point of view, it is necessary to take into account that the attenuation images are 2-D, thus they represent an average over the first 2–3 km below the surface. The estimated depths for scattered waves inferred by 3-D numerically simulated weighting functions (Del Pezzo *et al.* 2018) are concentrated in the first few kilometres of the crust when the source and receiver are both located at the surface and at a distance comparable with the average distances of the present data set. Moreover, ray tracing performed for velocity tomography shows ray coverage with the highest density in the first 2–3 km below the surface (see Díaz-Moreno *et al.* 2018).

According to previous studies carried out using the present technique and already mentioned above, it is more explanatory to consider the distribution of attenuation anomalies than it is to consider the absolute values; however, geological structures that are smaller than the cell dimension (5 km × 5 km) are invisible to our data set. To eliminate potential boundary distortions, after to perform the checkerboard test and identify the best resolved region, that is the area in which the method successfully retrieves the anomalies (see Fig. 4), we interpreted the data for an extracted smaller subregion.

5.2.1 Intrinsic attenuation anomalies

Fig. 6(a) shows the distribution of intrinsic attenuation anomalies in the Mt Etna region. As discussed, space averaged intrinsic Q values are low compared with most other volcanic regions; the areas characterized by strong intrinsic attenuation show changes of almost ±50 per cent with respect to the average. In this study, high

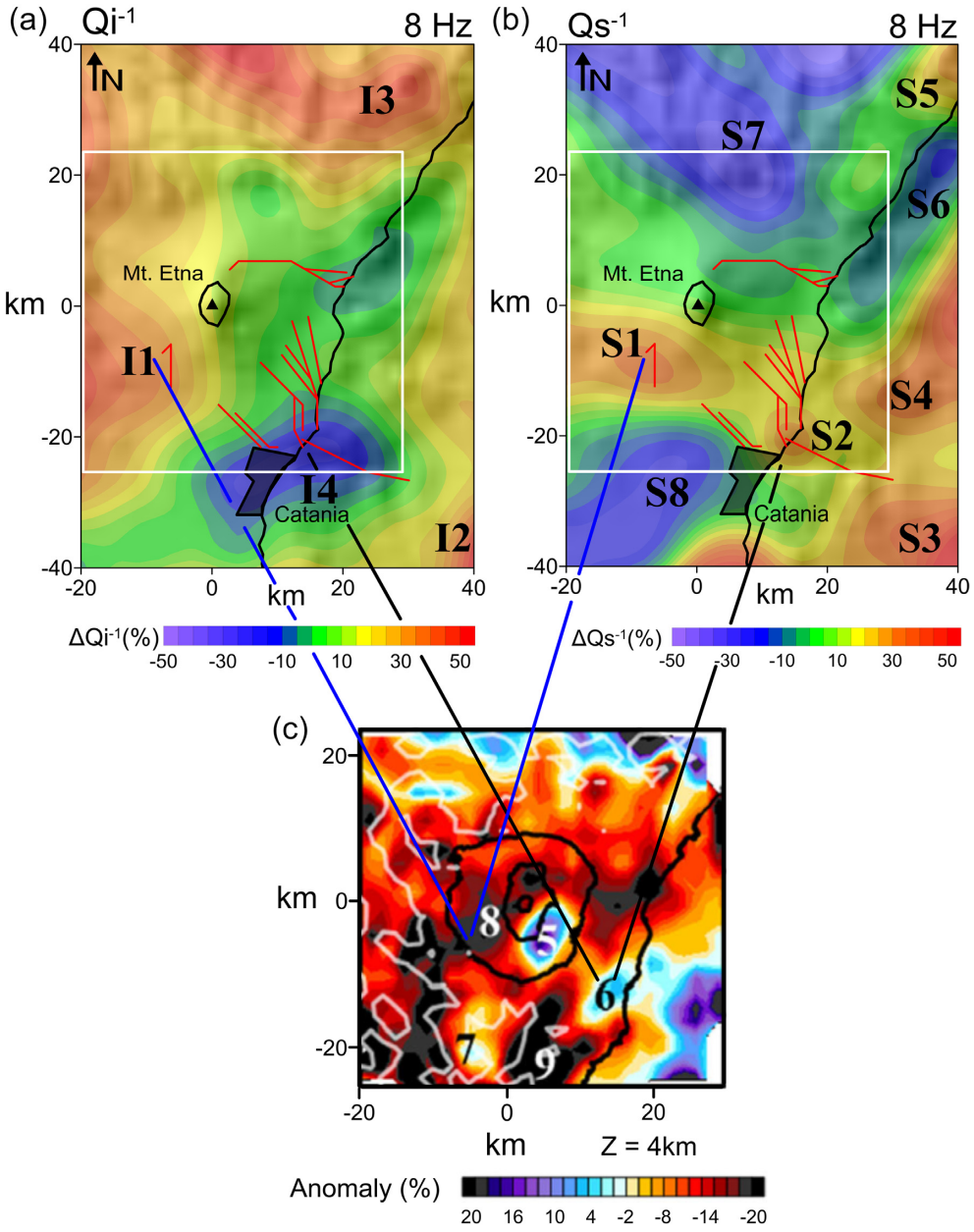

Figure 6. (a) *Qi*-1 and (b) *Qs*-1 anomaly maps obtained at 8 Hz for the best resolved region. The I and S labels correspond to the anomaly regions discussed in the text. Important fault systems are marked in red. (c) Modified map derived from Díaz-Moreno *et al.* (2018) for comparison of velocity and attenuation characteristics.

contrast regions were labelled as I1–I4, while I1–I3 represent high attenuation anomalies, and I4 is characterized by low attenuation values.

A high attenuation anomaly observed to the south west of Mt Etna (I1) is associated with the tectonic units of the Apenninic–Maghrebian chain, which are mainly formed by varicoloured clays and terrigenous turbiditic successions (Branca *et al.* 2011; Branca & Ferrara 2013). The high attenuation structure I2 is located in the southeastern part of the region and can be interpreted as the northern segments of the Alfeo-Etna Fault System (Polonia *et al.* 2017).

High attenuation area I3, located in the northern part of the volcanic edifice, reflects a high level of fracturing belonging to the Apenninic Maghrebian Chain and could represent prolongation of I1 towards the north (Cristofolini *et al.* 1979; Bianchi *et al.* 1987; Branca *et al.* 2011). The high attenuation values can be interpreted as the effects of a shallow fracture system associated with regional structural dynamics at the roof of this thrust system. Evidence for high levels of fracturing in this area is also presented in other studies (e.g. Barreca *et al.* 2018, and references therein). This region represents the Nebrodi-Peloritani Transition Zone, extending from the Aeolian Islands to the Ionian Sea. The area is characterized by complex fault systems in which NNW–SSE and WNW–ESE oriented fault segments (Lentini *et al.* 1995; Finetti *et al.* 1996) are overlapped by second-order N–S and NE–SW-striking faults (Giampiccolo & Tuvè 2018).

The most significant high-*Q* anomaly (I4; Fig. 6c) is located near of the city of Catania and correlates with a high velocity volume observed by Diaz Moreno *et al.* (2018). Owing to the

relatively low attenuation value, it may correspond to a highly consolidated body. Intrinsic attenuation is a reliable indicator of magmatic intrusions (e.g. De Siena *et al.* 2017) and therefore I4 is likely also associated to potential shallow magmatic bodies and submarine volcanism. These magmatic anomalies could be related to the earliest phase of volcanism and intruded into the Pleistocene marly clay succession of the Gela-Catania foredeep (Fig. 6a), as recently revealed in this sector by magnetic anomalies (Nicolosi *et al.* 2018).

5.2.2 Scattering attenuation anomalies

The scattering attenuation pattern is more heterogeneous than the intrinsic attenuation one (Figs 6a and b). We identified at least eight areas, denoted S1–S5 (high attenuation structures) and S6–S8 (low scattering attenuation).

A high scattering attenuation anomaly (S1) is located in the south west region of Mt Etna. In the last decades, several seismological studies linked the seismic activity occurring in this sector of the volcano to its recharging phases, leading to eruptive activity. In particular, the analysis of the seismicity occurred in this area before the 2001, 2002–2003 and 2008 lateral eruptions have been considered the fragile response of the Etna crust to magmatic intrusions mainly in the summit area and secondary in the upper South Rift zone (Bonaccorso *et al.* 2006; Sicali *et al.* 2015). In this area, the high degree of heterogeneity implied by the high scattering attenuation is confirmed by the presence of the shallow (up to 5 km bsl) Ragalna Fault System and South Volcanic Rift Zone (Azzaro *et al.* 2012). Moreover, from September 2017, this sector of the volcano was characterized by shallow seismicity that pre-dated and accompanied the December 2018 eruption (Gruppo Analisi Dati Sismici 2019). The S1 anomaly is located just to the south of the area in which Díaz-Moreno *et al.* (2018) and Aloisi *et al.* (2002) identified a shallow low-velocity anomaly region. It is suggested that this anomaly represents a magma storage volume on the basis of anomalous *b* values (Murru *et al.* 1999) and ground deformation inversions (Nunnari & Puglisi 1994; Bonaccorso *et al.* 1996).

Another high scattering anomaly is located north of Catania (S2). This anomaly could be associated with the Fiadanca, Santa Tecla and Timple faults (Azzaro *et al.* 2012), which are linked to the lithospheric dextral transtensional North Alfeo fault system (Gutscher *et al.* 2016, 2017; Polonia *et al.* 2017) dissecting the lower SE flank of the volcano.

In the southeastern area, at the same location as the I2 anomaly, a high scattering anomaly is also observed (S3). Following Polonia *et al.* (2017), we interpret this anomaly as a segment of the Alfeo-Etna fault system. The S4 high scattering anomaly is located east of Mt Etna, offshore and beneath the Ionian Sea. This anomaly can be interpreted as a highly fractured region where the Ionian Fault and Alfeo-Etna fault system converge (Polonia *et al.* 2017). Near I3, a high scattering attenuation anomaly is also observed (S5). As such, this area is characterized by both high intrinsic and scattering attenuation values and can be interpreted as a volume with a very high level of fracturing. The S6 anomaly is located northeast of Mt Etna, and partly extends offshore. This region could be connected to the large low scattering anomaly of S7, and both can be related to shallow (1–2 km bsl) carbonate units of the external thrust system (Branca *et al.* 2011). Finally, the S8 anomaly is located to the west of Catania. Owing to its scattering behaviour it can be interpreted as a homogeneous body; this interpretation is consistent with the results of Branca *et al.* (2011), who identified compact carbonates of the Hyblean Plateau covered by the Catania-Gela foredeep sediments at a depth of approximately 1 km bsl (Torelli *et al.* 1998).

6 CONCLUSIONS

This work provides new evidence of the structural complexity of the Mt Etna volcanic area. The data set used comprised waveforms recorded during the TOMO-ETNA experiment, with nearly uniform and homogeneous ray coverage. The methodology used in this study, which had not been applied to this area before, allowed us to characterize intrinsic and scattering attenuation in the region, which in turn supports an improved geological interpretation. Mt Etna appears as a single domain, for which the shallowest rocks (2–3 km bsl) have the highest intrinsic and scattering attenuation. However, attenuation beneath the Mt Etna area is dominated by scattering effects, which are strong enough to fully justify the use of diffusion approximation for the energy transport equation.

From the scattering attenuation anomaly map, it is possible to infer that Mt Etna volcano is situated between two large tectonic regions that dynamically stress and fracture the area. Good correlations between attenuation and velocity anomalies confirm that the method is a suitable complement to ordinary seismic velocity tomography.

The most prominent result is a strong correlation among the occurrence of seismicity, volcanic activity, and high attenuation effects in the southwestern area of Mt Etna (named S1). In conclusion, this work supports the hypothesis that the SW flank dynamics, including the summit area and upper South Rift Zone, are linked to magma recharge during recent decades.

ACKNOWLEDGEMENTS

This work was partially funded by the Spanish Mineco Project KNOWAVES (TEC2015-68752-R1) and the Grupo de Investigación Junta de Andalucia (RNM104). LZ was partially supported by the European Union Horizon 2020 Research and Innovation Programme under a Marie Sklodowska-Curie Grant (agreement No. 798480). JP was partially supported by the Juan de la Cierva restarting program. We would like to thank all participants of the TOMO-ETNA experiment. We would like to thanks the contribution of Dr Luca De Siena and an anonymous reviewer that have largely improved the quality of the present manuscript. Author Contributions: Jesús M. Ibáñez and Janire Prudencio coordinated the work and developed and performed the main redaction control and data acquisition procedure; Ignacio Castro-Melgar and Janire Prudencio processed the data: Ornella Cocina, Luciano Zuccarello and Stefano Branca performed data interpretation; Edoardo Del Pezzo developed and analysed the algorithms and performed data analysis quality control. All authors participated in preparation of the manuscript. English language editing was performed by Tornillo Scientific, UK.

REFERENCES

Alparone, S., Barberi, G., Cocina, O., Giampiccolo, E., Musumeci, C. & Patanè, D., 2012. Intrusive mechanism of the 2008–2009 Mt. Etna eruption: constraints by tomographic images and stress tensor analysis, *J. Volc. Geotherm. Res.*, **229,** 50–63.

Aki, K. & Chouet, B., 1975. Origin of coda waves: source, attenuation, and scattering effects, *J. geophys. Res.*, **80**(23), doi:10.1029/JB080i023p03322.

Akinci, A., Del Pezzo, E. & Ibanez, J.M., 1995. Separation of scattering and intrinsic attenuation in southern Spain and western Anatolia (Turkey), *Geophys. J. Int.,* **121**(2), 337–353.

Aloisi, M., Cocina, O., Neri, G., Orecchio, B. & Privitera, E., 2002. Seismic tomography of the crust underneath the Etna volcano, Sicily, *Phys. Earth planet. Inter.,* **134,** 139–155.

Azzaro, R., Branca, S., Gwinner, K. & Coltelli, M., 2012. The volcano-tectonic map of Etna volcano, 1: 100.000 scale: an integrated approach based on a morphotectonic analysis from high-resolution DEM constrained by geologic, active faulting and seismotectonic data, *Ital. J. Geosci.,* **131**(1), 153–170.

Barreca, G., Branca, S. & Monaco, C., 2018. Three-dimensional modeling of mount etna volcano: volume assessment, trend of eruption rates, and geodynamic significance, *Tectonics,* **37**(3), 842–857.

Bianchi, F., Carbone, S., Grasso, M., Invernizzi, G., Lentini, F., Longaretti, G., Merlini, S. & Mostardini, F., 1987. Sicilia orientale: profile geologico Nebrodi-Iblei, *Mem. Soc. Geol. It.,* **38,** 429–458.

Bonaccorso, A., Ferucci, F., Patanè, D. & Villari, L., 1996. Fast deformation processes and eruptive activity at Mr. Etna (Italy), *J. geophys. Res.,* **101,** 17 467–17 480.

Bonaccorso, A., Bonforte, A., Guglielmino, F., Palano, M. & Puglisi, G., 2006. Composite ground deformation pattern forerunning the 2004–2005 Mount Etna eruption, *J. geophys. Res.,* **111,** B12, doi:10.1029/2005JB004206.

Branca, S. & Ferrara, V., 2013. The morphostructural setting of Mount Etna sedimentary basement (Italy): implications for the geometry and volume of the volcano and its flank instability, *Tectonophysics,* **586**(26), 46–64.

Branca, S., Coltelli, M., Groppelli, G. & Lentini, F., 2011. Geological map of Etna volcano, 1: 50,000 scale, *Ital. J. Geosci.,* **130**(3), 265–291.

Carmona, E., Almendros, J., Alguacil, G., Soto, J. I., Luzón, F. & Ibáñez, J. M., 2015. Identification of T-Waves in the Alboran Sea, *Pure appl. Geophys.,* **172**(11), 3179–3188.

Chiarabba, C., De Gori, P. & Patanè, D., 2004. The Mt. Etna plumbing system: the contribution of seismic tomography, *Washington DC American Geophysical Union Geophysical Monograph Series,* **143,** 191–204.

Coltelli, M., Cavallaro, D., Firetto Carlino, M., Cocchi, L., Muccini, F., D'Aessandro, A. & Patanè, D., 2016. The marine activities performed within the TOMO-ETNA experiment, *Ann. Geophys.,* **59**(4), doi:10.4401%2Fag-7081.

Cristofolini, R., Lentini, F., Patanè, G. & Rasà, R., 1979. Integrazione di dati geologici, geofisici e petrologici per la stesura di un profilo crostale in corrispondenza dell'Etna, *Boll. Soc. Geol. It.,* **98**(2), 239–247.

Dainty, A.M. & Toksöz, M.N., 1981. Seismic codas on the Earth and the Moon: a comparison, *Phys. Earth planet. Int.,* **26**(4), 250–260.

De Gori, P., Chiarabba, C. & Patanè, D., 2005. Qp structure of Mount Etna: constraints for the physics of the plumbing system, *J. geophys. Res.,* **110**(B5), doi:10.1029/2003JB002875.

De Siena, L., Thomas, C., Waite, G.P., Moran, S.C. & Klemme, S., 2014. Attenuation and scattering tomography of the deep plumbing system of Mount St. Helens, *J. geophys. Res.,* **119**(11), 8223–8238.

De Siena, L., Calvet, M., Watson, K.J., Jonkers, A.R.T. & Thomas, C., 2016. Seismic scattering and absorption mapping of debris flows, feeding paths, and tectonic units at Mount St. Helens volcano, *Earth planet. Sci. Lett.,* **442,** 21–31.

De Siena, L., Amoruso, A., Del Pezzo, E., Wakeford, Z., Castellano, M. & Crescentini, L., 2017. Space-weighted seismic attenuation mapping of the aseismic source of Campi Flegrei 1983–1984 unrest, *Geophys. Res. Lett.,* **44**(4), 1740–1748.

Del Pezzo, E., 2008. Chapter 13 Seismic Wave Scattering in Volcanoes, in *Earth Heterogeneity and Scattering Effects on Seismic Waves,* Vol. **50,** 353–371, ed. Dmowska, R, Elsevier, doi:10.1016/S0065-2687(08)00013-7.

Del Pezzo, E., Ibanez, J., Prudencio, J., Bianco, F. & De Siena, L., 2016. Absorption and scattering 2-D volcano images from numerically calculated space-weighting functions, *Geophys. J. Int.,* **206**(2), 742–756.

Del Pezzo, E., De La Torre, A., Bianco, F., Ibanez, J., Gabrielli, S. & De Siena, L., 2018. Numerically calculated 3D space-weighting functions to image crustal volcanic structures using diffuse coda waves, *Geoscience,* **8**(5), 175, doi:10.3390/geosciences8050175.

Del Pezzo, E., Giampiccolo, E., Tuvè, T., Di Grazia, G., Gresta, S. & Ibanez, J., 2019. Study of the regional pattern of intrinsic and scattering seismic attenuation in Eastern Sicily (Italy) from local earthquakes, *Geophys. J. Int.,* **218,** 2, 1456–1468.

Díaz-Moreno, A., Barberi, G., Cocina, O., Koulakov, I., Scarfì, L., Zuccarello, L. & Ibáñez, J.M., 2018. New insights on Mt. Etna's crust and relationship with the regional tectonic framework from joint active and passive P-wave seismic tomography, *Surv. Geophys.,* **39**(1), 57–97.

Finetti, I., Lentini, F., Carbone, S. & Catalano, S., 1996. Il sistema Appennino Meridionale-Arco Calabro-Sicilia nel Mediterraneo Centrale: studio geologico-geofisico, *Boll. Soc. Geol. It.,* **115,** 529–559.

Flatté, S.M., Dashen, R., Munk, W., Watson, K. & Zachariasen, F., 1979. *Sound Transmission Through a Fluctuating Ocean,* Cambridge Univ. Press.

García-Yeguas, A., Koulakov, I., Ibáñez, J.M. & Rietbrock, A., 2012. High resolution 3D P wave velocity structure beneath Tenerife Island (Canary Islands, Spain) based on tomographic inversion of active-source data, *J. geophys. Res.,* **117**(B9), doi:10.1029/2011JB008970.

Giampiccolo, E. & Tuvè, T., 2018. Regionalization and dependence of coda Q on frequency and lapse time in the seismically active Peloritani region (northeastern Sicily, Italy), *J. Seismol.,* **22**(4), 1059–1074.

Gruppo Analisi Dati Sismici, 2019. *Catalogo dei terremoti della Sicilia Orienta–e - Calabria Meridionale (1999–2019),* INGV, Catania, http://www.ct.ingv.it/ufs/analisti/catalogolist.php.

Gutscher, M.A., Dominguez, S., de Lepinay, B.M., Pinheiro, L., Gallais, F., Babonneau, N. & Rovere, M., 2016. Tectonic expression of an active slab tear from high-resolution seismic and bathymetric data offshore Sicily (Ionian Sea), *Tectonics,* **35**(1), 39–54.

Gutscher, M.A., Kopp, H., Krastel, S., Bohrmann, G., Garlan, T., Zaragosi, S. & San Pedro, L., 2017. Active tectonics of the Calabrian subduction revealed by new multi-beam bathymetric data and high-resolution seismic profiles in the Ionian Sea (Central Mediterranean), *Earth planet. Sci. Lett.,* **461,** 61–72.

Hoshiba, M., 1991. Simulation of multiple-scattered coda wave excitation based on the energy conservation law, *Phys. Earth planet. Int.,* **67**(1–2), 123–136.

Ibáñez, J.M., Morales, J., De Miguel, F., Vidal, F., Alguacil, G. & Posadas, A.M., 1991. Effect of a sedimentary basin on estimations of Qc and QLg, *Phys. Earth planet. Int.,* **66**(3–4), 244–252.

Ibáñez, J.M., Prudencio, J., Díaz-Moreno, A., Patanè, D., Puglisi, G., Lühr, B.G. & Del Pezzo, E., 2016a. The TOMO-ETNA experiment: an imaging active campaign at Mt. Etna volcano. Context, main objectives, working-plans and involved research projects, *Ann. Geophys.,* **59**(4), 0426, doi:10.4401/ag-7079.

Ibáñez, J.M., Díaz-Moreno, A., Prudencio, J., Patanè, D., Zuccarello, L., Cocina, O. & Bianco, F., 2016b. TOMO-ETNA experiment at Etna volcano: activities on land, *Ann. Geophys.,* **59**(4), doi:10.4401/ag-7080.

Jensen, F.B., Kuperman, W.A., Porter, M.B. & Schmidt, H., 1994. Computational Ocean Acoustics. AIP Series in Modern Acoustics and Signal Processing.

Koulakov, I., Maksotova, G., Jaxybulatov, K., Kasatkina, E., Shapiro, N.M., Luehr, B.G. & Al-Arifi, N., 2016. Structure of magma reservoirs beneath Merapi and surrounding volcanic centers of Central Java modeled from ambient noise tomography, *Geochem. Geophys. Geosyst.,* **17**(10), 4195–4211.

Lentini, F., Carbone, S., Catalano, S., Di Stefano, A., Gargano, C., Romeo, M. & Vinci, G., 1995. Sedimentary evolution of basins in mobile belts: examples from the Tertiary terrigenous sequences of the Peloritani Mountains (NE Sicily), *Terra Nova,* **7**(2), 161–170.

Martı´nez-Arévalo, C., Bianco, F., Ibáñez, J. M. & Del Pezzo, E. 2003. Shallow seismic attenuation and shear-wave splitting in the short period range of Deception Island volcano (Antarctica), *J. Volc. Geotherm. Res.,* **128**(1-3), 89–113.

Martínez-Arévalo, C., Patanè, D., Rietbrock, A. & Ibánez, J.M., 2005. The intrusive process leading to the Mt. Etna 2001 flank eruption:

constraints from 3-D attenuation tomography, *Geophys. Res. Lett.,* **32**(21), doi:10.1029/2005GL023736.
Mayeda, K., Koyanagi, S., Hoshiba, M., Aki, K. & Zheng, Y., 1992. A comparative study of scattering, intrinsic, and coda Q−1 for Hawaii, Long Valley and Central California between 1.5 and 15 Hz, *J. geophys. Res.,* **97,** 6643–6659.
Medwin, H., 1975. Speed of sound in water: a simple equation for realistic parameters, *J. acoust. Soc. Am.,* **58**(6), 1318–1319.
Munk, W., Worcester, P. & Wunsch, C., 1995. *Ocean Acoustic Tomography*. Cambridge Univ. Press.
Murru, M., Montuori, C., Wyss, M. & Privitera, E., 1999. The locations of magma chambers at Mt. Etna, Italy, mapped by b-values, *Geophys. Res. Lett.,* **26**(16), doi:10.1029/1999GL900568.
Nicolosi, I., D'Ajello Caracciolo, F., Branca, S., Speranza, F. & Chiappini, M., 2018. Unravelling Mount Etna's early eruptive history by three-dimensional magnetic modeling, *Bull. geol. Soc. Am.,* **130,** 9–10, 1664–1674.
Northrup, J. & Colborn, J. G., 1974. Sofar channel axial sound speed and depth in the Atlantic Ocean, *J. geophys. Res.,* **79,** 5633–5641.
Nunnari, G. & Puglisi, G., 1994. The global positioning system as a useful technique for measuring ground deformations in volcanic areas, *J. Volc. Geotherm. Res.,* **61**(3/4), 267–280.
Patanè, D., Barberi, G., Cocina, O., De Gori, P. & Chiarabba, C., 2006. Time-resolved seismic tomography detects magma intrusions at Mount Etna, *Science,* **313**(5788), 821–823.
Polonia, A., Torelli, L., Gasperini, L., Cocchi, L., Muccini, F., Bonatti, E. & Carlini, M., 2017. Lower plate serpentinite diapirism in the Calabrian Arc subduction complex, *Nat. Commun.,* **8**(1), 2172, doi:10.1038/s41467-017-02273-x.
Prudencio, J., Del Pezzo, E., García-Yeguas, A. & Ibáñez, J.M., 2013a. Spatial distribution of intrinsic and scattering seismic attenuation in active volcanic islands–I: model and the case of Tenerife Island, *Geophys. J. Int.,* **195**(3), 1942–1956.
Prudencio, J., Ibáñez, J.M., García-Yeguas, A., Del Pezzo, E. & Posadas, A.M., 2013b. Spatial distribution of intrinsic and scattering seismic attenuation in active volcanic islands–II: deception Island images, *Geophys. J. Int.,* **195**(3), 1957–1969.
Prudencio, J., De Siena, L., Ibáñez, J.M., Del Pezzo, E., Garcia-Yeguas, A. & Diaz-Moreno, A., 2015a. The 3D attenuation structure of deception Island (Antarctica), *Surv. Geophys.,* **36**(3), 371–390.
Prudencio, J., Ibáñez, J.M., Del Pezzo, E., Martí, J., García-Yeguas, A. & De Siena, L., 2015b. 3D attenuation tomography of the volcanic island of Tenerife (Canary Islands), *Surv. Geophys.,* **36**(5), 693–716.
Prudencio, J., Del Pezzo, E., Ibáñez, J.M., Giampiccolo, E. & Patané, D., 2015c. Two-dimensional seismic attenuation images of Stromboli Island using active data, *Geophys. Res. Lett.,* **42**(6), 1717–1724.
Prudencio, J., Aoki, Y., Takeo, M., Ibáñez, J.M., Del Pezzo, E. & Song, W., 2017a. Separation of scattering and intrinsic attenuation at Asama volcano (Japan): Evidence of high volcanic structural contrasts, *J. Volc. Geotherm. Res.,* **333,** 96–103.
Prudencio, J., Taira, T., Aoki, Y., Aoyama, H. & Onizawa, S., 2017b. Intrinsic and scattering attenuation images of Usu volcano, Japan, *B. Volcanol.,* **79**(4), 29, doi:10.1007/s00445-017-1117-9.
Prudencio, J., Manga, M. & Taira, T., 2018. Subsurface Structure of Long Valley Caldera Imaged With Seismic Scattering and Intrinsic Attenuation, *J. geophys. Res.,* **123**(7), 5987–5999.
Salon, S., Crise, A., Picco, P., De Marinis, E. & Gasparini, O., 2003. Sound speed in the Mediterranean Sea: an analysis from a climatological data set, *Ann. Geophys.,* **21,** 833–846.
Sanborn, Christopher J. & Cormier, Vernon F. 2018. Modelling the blockage of Lg waves from three-dimensional variations in crustal structure, *Geophys. J. Int.* **214**(20), 1426–1440.
Sato, H., Fehler, M.C. & Maeda, T., 2012. *Seismic Wave Propagation and Scattering in the Heterogeneous Earth,* Vol. **496,** Springer.
Sicali, S., Barberi, G., Cocina, O., Musumeci, C. & Patanè, D., 2015. Volcanic unrest leading to the July-August 2001 lateral eruption at Mt. Etna: seismological constraints, *J. Volc. Geotherm. Res.,* **304,** 11–23.
Taburni, D., 2011. Elaborazione e sperimentazione di un modello matematico di propagazione dell'inquinamento acustico subacqueo, nell'ambito del progetto GIONHA "Governance and Integrated Observation of marine Natural Habitat", Technical Report CNR-IDASC, http://www.gionha.it/risorse/pubblicazioni/report/.
Torelli, L., Grasso, M., Mazzoldi, G. & Peis, D., 1998. Plio–Quaternary tectonic evolution and structure of the Catania foredeep, the northern Hyblean Plateau and the Ionian shelf (SE Sicily), *Tectonophysics,* **298,** 209–221.
Wegler, U., 2003. Analysis of multiple scattering at Vesuvius volcano, Italy, using data of the TomoVes active seismic experiment, *J. Volc. Geotherm. Res.,* **128**(1–3), 45–63.
Wegler, U. & Lühr, B.G., 2001. Scattering behaviour at Merapi volcano (Java) revealed from an active seismic experiment, *Geophys. J. Int.,* **145**(3), 579–592, doi:10.1046/j.1365-246x.2001.01390.x.
Wu, R., 1985. Multiple scattering and energy transfer of seismic waves—separation of scattering effect from intrinsic attenuation — I. Theoretical modelling, *Geophys. J. R. Astr. Sci.,* **82**(1), doi:10.1111/j.1365-246X.1985.tb05128.x.
Yamamoto, M. & Sato, H., 2010. Multiple scattering and mode conversion revealed by an active seismic experiment at Asama volcano, Japan, *J. geophys. Res.: Solid Earth,* **115** (B7).
Zandomeneghi, D., Barclay, A., Almendros, J., Ibañez Godoy, J.M., Wilcock, W.S. & Ben-Zvi, T., 2009. Crustal structure of Deception Island volcano from P wave seismic tomography: tectonic and volcanic implications, *J. geophys. Res.* **114**(B6), doi:10.1029/2008JB006119.
Zieger, T., Sens-Schönfelder, C., Ritter, J.R., Lühr, B.G. & Dahm, T., 2016. P-wave scattering and the distribution of heterogeneity around Etna volcano, *Ann. Geophys.,* **59**(4), 0432.

APPENDIX A: RESOLUTION FUNCTION

To simplify the mathematical notation, we removed the dependence of function w (eq. 1) on space, source, and receiver coordinates, and denoted the weighting functions (each normalized for their maximum) by w_{ij}, where i is the event–source index and j represents the jth pixel of coordinates x,y; i spans from 1 to N, where N is the number of source–receiver couples in the data set; and j spans from 1 to M, where M is the number of pixels (square regions or cells in which the input image is divided).

We further denote with q_i the Q-value (or its inverse) measured for the ith source–receiver couple, and with q_j the output of the mapping method for the jth pixel. In this simplified notation, the mapping method (eq. 9) yields

$$q_j = \frac{\sum_i q_i w_{ij}}{\sum_i w_{ij}} . \tag{A1}$$

Assuming that the standard deviation, σ, is the same for all measures of q_i and by applying the error propagation equation to eq. (A1) we obtain

$$\sigma_{qj}^2 = \frac{\sigma^2 \sum w_{ij}^2}{(\sum w_{ij})^2} . \tag{A2}$$

Finally, we can reasonably assume that the quantity $\frac{\sigma^2}{\sigma_{qj}}$ represents an estimate of the resolution of the method. In other words, pixels showing smaller resolution should be associated with higher error and vice versa. Resolution at the ith pixel is thus given by

$$R_j = \left(\frac{(\sum w_{ij})^2}{\sum w_{ij}^2}\right)^{1/2}, \tag{A3}$$

where R_j represents all pixels in Fig. 5.

APPENDIX B: Qi^{-1} AND Qs^{-1} ANOMALY MAPS

Qi^{-1} and Qs^{-1} anomaly maps for 4–24 Hz are represented in Fig. B1.

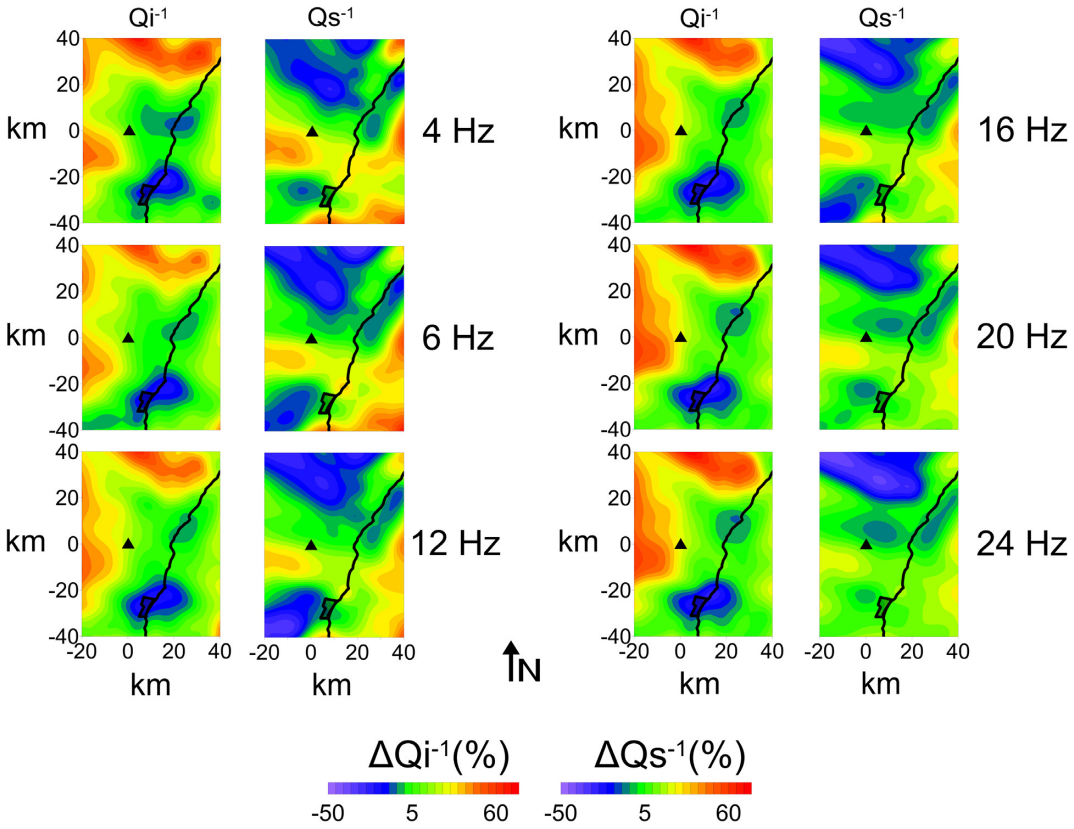

Figure B1. *Qi*-1 and *Qs*-1 anomaly maps for all analysed frequency bands.